



## Article

# Precision Manufacturing in China of Replication Mandrels for Ni-Based Monolithic Wolter-I X-ray Mirror Mandrels

Jiadao Xue <sup>1</sup>, Bo Wang <sup>1,\*</sup>, Qiuyan Liao <sup>1</sup>, Kaiji Wu <sup>1</sup>, Yutao Liu <sup>1</sup>, Yangong Wu <sup>1</sup>, Wentao Chen <sup>1</sup>, Zheng Qiao <sup>1</sup>, Yuan Jin <sup>1</sup>, Fei Ding <sup>1,\*</sup>, Dianlong Wang <sup>1</sup>, Langping Wang <sup>1</sup>, Guo Li <sup>2</sup>, Yanji Yang <sup>3</sup> and Yong Chen <sup>3</sup>

<sup>1</sup> Center for Precision Engineering, Harbin Institute of Technology, No. 92 Xidazhijie Street, Harbin 150001, China; 15765517664@163.com (J.X.); hpfw15545007909@163.com (K.W.)

<sup>2</sup> School of Mechanical and Power Engineering, Harbin University of Science and Technology, No. 52 Xuefu Street, Harbin 150080, China

<sup>3</sup> Institute of High Energy Physics, Chinese Academy of Sciences (CAS), 19B Yuquan Road, Beijing 100049, China

\* Correspondence: bradywang@hit.edu.cn (B.W.); fei.ding@hit.edu.cn (F.D.)

**Abstract:** The X-ray satellite “Einstein Probe” of the Chinese Academy of Sciences (CAS) was successfully launched on 9 January 2024 at 15:03 Beijing Time from the Xichang Satellite Launch Center in China with a “Long March-2C” rocket. The Einstein Probe is equipped with two scientific X-ray telescopes. One is the Wide-field X-ray Telescope (WXT), which uses lobster-eye optics. The other is the Follow-up X-ray Telescope (FXT), a Wolter-I type telescope. These telescopes are designed to study the universe for high-energy X-rays associated with transient high-energy phenomena. The FXT consists of two modules based on 54 thin X-ray Wolter-I grazing incidence Ni-replicated mirrors produced by the Italian Media Lario company, as contributions from the European Space Agency and the Max Planck Institute for Extraterrestrial Physics (MPE), which also provided the focal-plane detectors. Meanwhile, the Institute of High Energy Physics (IHEP), together with the Harbin Institute of Technology and Xi’an Institute of Optics and Precision Mechanics, has also completed the development and production of the structural and thermal model (STM), qualification model (QM) and flight model (FM) of FXT mirrors for the Einstein Probe (EP) satellites for demonstration purposes. This paper introduces the precision manufacturing adopted in China of Wolter-I X-ray mirror mandrels similar to those used for the EP-FXT payload. Moreover, the adopted electroformed nickel replication process, based on a chemical nickel–phosphorus alloy, is reported. The final results show that the surface of the produced mandrels after demolding and the internal surface of the mirrors have been super polished to the roughness level better than 0.3 nm RMS and the surface accuracy is better than 0.2  $\mu\text{m}$ , and the mirror angular resolution for single mirror shells may be as good as 17.3 arcsec HPD (Half Power Diameter), 198 arcsec W90 (90% Energy Width) @1.49 keV (Al-K line). These results demonstrate the reliability and advancement of the process. As the first efficient X-ray-focusing optics manufacturing chain established in China, we successfully developed the first focusing mirror prototype that could be used for future X-ray satellite payloads.

**Keywords:** follow-up X-ray telescope; electroformed nickel replication; Wolter-I X-ray mirror mandrels; precision manufacturing



**Citation:** Xue, J.; Wang, B.; Liao, Q.; Wu, K.; Liu, Y.; Wu, Y.; Chen, W.; Qiao, Z.; Jin, Y.; Ding, F.; et al. Precision Manufacturing in China of Replication Mandrels for Ni-Based Monolithic Wolter-I X-ray Mirror Mandrels. *Aerospace* **2024**, *11*, 849. <https://doi.org/10.3390/aerospace11100849>

Academic Editor: Hyun-Ung Oh

Received: 31 May 2024

Revised: 11 October 2024

Accepted: 13 October 2024

Published: 15 October 2024



**Copyright:** © 2024 by the authors. Licensee MDPI, Basel, Switzerland. This article is an open access article distributed under the terms and conditions of the Creative Commons Attribution (CC BY) license (<https://creativecommons.org/licenses/by/4.0/>).

## 1. Introduction

Astronomy has entered the multi-messenger era. The universe is filled with a large number of transient sources and explosive celestial bodies, whose activities radiate huge high-energy rays such as X-rays and  $\gamma$  radiation. The nature of the mysterious Dark Energy, which is driving the universe apart, is one of the most exciting questions facing astronomy and physics today. It could be the vacuum energy, corresponding to the Cosmological Constant in Einstein’s theory of General Relativity, or it could be a time-varying energy field.

Answering this question could be the starting point of a fundamental revolution in physics. X-rays are about 1000 times more energetic than visible light photons and are produced by violent explosions and high-temperature astronomical environments. Instead of the familiar steady stars, the sky would seem to be filled with exotic stars, active galaxies, and hot supernova remnants. Transient sources and explosive celestial bodies in the universe need to be observed by X-rays. The Einstein Probe (EP) mission is one of the projects of the Strategic Priority Program on Space Science (II) [1]. The EP is a satellite dedicated to time-domain astronomy to study the universe for high-energy X-rays associated with transient high-energy phenomena [2]. The Follow-up X-ray Telescope (FXT) is one of the key payloads onboard the EP. After the observation data obtained by the FXT payload are processed by the scientific application system, the final scientific data will provide the position, energy, time and other information of X-ray photons for scientists to image, locate, and perform flow intensity, light change and energy spectrum analyses. The FXT is a Wolter-I-type X-ray focusing telescope equipped with two telescope modules (focal length 1.6 m), with a total effective area of  $\sim 600 \text{ cm}^2$  at 1.25 keV and an energy range of 0.3–10 keV [3]. The main designed characteristics of the FXT are shown in Table 1. One of the FXT mirror assemblies is provided by ESA (Paris, France) and has a design similar to that of eROSITA [4,5]. For the other FXT mirror, there are two parallel solutions. One is to use the flight spare mirror of eROSITA, and the other one is to develop and manufacture in China [3]. In 2020, IHEP, together with the Harbin Institute of Technology and the Xi'an Institute of Optics and Precision Mechanics, had manufactured the thermal-control model (TCM) of the FXT mirror assembly parallelly. The TCM has participated in the thermal balance test of the whole satellite. Considering the maturity of existing technologies in China, some of the corresponding indicators are somewhat inclusive. The angular resolution of the entire mirror module with the 54 shells together is required to be better than 2 arcmin with the goal of being better than 30 arcsec.

**Table 1.** Characteristics of the FXT [3,4].

Parameter	Requirements
Number of modules	2
Number of shells per module	45
Field of View	$1 \text{ deg}^2$
Effective area	$600 \text{ cm}^2$ @ 1.25 keV
Angular resolution (Half Energy Width, HEW)	$\leq 30''$ (on axis; FXT system level); $\leq 2'$ basic requirement for IHEP group
Energy resolution	120 eV @ 1.25 keV
Energy range	0.5–8 keV
Focal length	$1600 \pm 10 \text{ mm}$
Maximum and minimum diameter of the shells	357.6 mm (outermost shell)–76.7 mm (innermost shell)
Total mirror length	300 mm
Thickness of the shells	0.55 mm (outermost shell)–0.20 mm (innermost shell)

The focusing quality of the mirror is directly correlated with the mandrel machining accuracy in the EP-FXT mission, which is produced by utilizing the electroformed nickel replication method. In addition to the shape error, the mid- and high-spatial frequency inaccuracies have a significant impact on the focusing mirror's optical performance. The Wolter-I focusing mirror is an integral structure composed of two coaxial confocal parts, which are paraboloid and hyperboloid. Numerous research institutes across the globe have been studying the production process of the nesting Wolter-I-type grazing incident X-ray focusing mirror in great detail since the 1970s. Direct polishing [6], wafer splicing [7], glass sheet thermal collapse [8], and electroforming replication [9–12] are the main manufacturing techniques that have been developed.

The nickel electroforming replication is used to obtain X-ray mirror shells from precisely machined and polished mandrels (representing the X-ray mirrors' negative shape).

This approach for multi-shell X-ray optics was first developed in Italy for the production of the X-ray mirrors of the Beppo-SAX satellites more than 35 years ago by INAF (Rome, Italy) and the Media Lario company (Bosisio Parini, Italy) in the early 1990s [13]. The electroformed nickel replication process creates thin structural shells with high precision, low surface roughness, and a low production cost. This process has been widely utilized for manufacturing nested X-ray focusing mirrors. It has been adopted for various X-ray missions optics manufacturing projects (e.g., Beppo SAX for ASI (Rome, Italy), XMM Newton for ESA, JET-X/SWIFT for NASA (Washington, DC, USA), eROSITA for MPE (Munich, Germany), IXPE for NASA, the Einstein Probe for CAS-ESA, and eXTP for CAS (Beijing, China)). Media Lario, INAF, and NASA/MSFC have all described and utilized this technology in their papers [14–17]. This method has become one of the most advanced ways to produce X-ray focusing mirrors in terms of precision and production efficiency.

This paper mainly introduces the precision manufacturing of Wolter X-ray mirror mandrels for the EP-FXT mission, especially the fabrication of the mandrel, which directly affects the final optical performance of the focusing mirror. The processes of single-point diamond turning and full-aperture super-smooth pitch polishing are adopted to achieve the required surface shape and the sub-nanoscale super-smooth surfaces, respectively, for the EP-FXT mission. However, ultra-smooth polishing of molds can lead to collapses at the ends of the mold and in the middle of the interface, which can be replicated by the mirrors [16]. The discontinuity of the face profile at the mold edges and junctions leads to an increase in the polishing pressure and removal which caused slumping, and the form error, depending on the polishing process, is generally around 1  $\mu\text{m}$  or higher. The edge effect error on the imaging system is disastrous for the degradation of W90 (90% Energy Width). Bonnet polishing can achieve an ultra-smooth surface texture using a flexible inflated tool. In this study, a combined polishing process chain consisting of pitch polishing and bonnet polishing was proposed, in which bonnet polishing plays a role in figure accuracy and pitch polishing plays a role in the rapid surface smoothing of the mandrels. The final results show that the surface roughness of the focusing mirror mandrels is less than 0.3 nm RMS (500  $\mu\text{m} \times 500 \mu\text{m}$  with white-light interferometer), the surface profile accuracy is better than 0.2  $\mu\text{m}$ , and the angular resolution of a single shell #24 (diameter is 183.56 mm and thickness is 0.31 mm) is 17.3 "HPD, 197.8" W90 @1.49 keV, which verifies the reliability and advancement of the process.

## 2. The Replication Process Route Adopted in the Study

### 2.1. Overall Technical Route

The overall technical route of the electroforming replication process of X-ray focusing lenses is shown in Figure 1. The mandrel mold substrate is usually made of the aluminum alloy shown in Figure 1a, and a nickel–phosphorus alloy is chemically plated on its surface as shown in Figure 1b. Since the surface accuracy and surface roughness of the mandrel will be directly copied to the internal reflection surface of the mirror through electroforming, which determines the imaging quality, ultra-precision machining of the mandrel is a key process, which specifically includes two steps: the ultra-precision turning shown in Figure 1c and the ultra-smooth polishing shown in Figure 1d. After the metrology shown in Figure 1e and the cleaning shown in Figure 1f, the mandrel is coated with a gold film of hundreds of nanometers by magnetron sputtering as an X-ray reflection film as shown Figure 1g. Over the gold layer, a special stress-free NiCo shell is electroformed to approximately 0.2~1 mm thick as shown in Figure 1h. With the different thermal expansion coefficients of the mandrel and the mirror material, they are separated by cooling and shrinking as shown in Figure 1i.

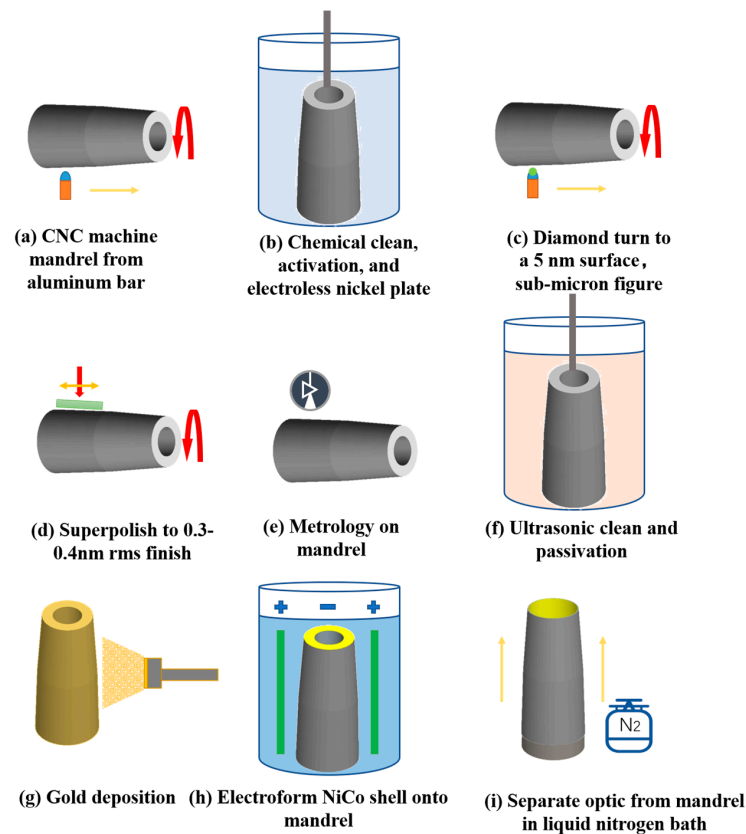


**Figure 1.** Focus mirror of electroformed nickel replication process flow.

## 2.2. Chemical Plating with Nickel–Phosphorus Alloy

The phosphorus concentration of the electroless nickel–phosphorus alloy layer is about 10% and it has an amorphous structure. This mixture performs exceptionally well in ultraprecision machining, enabling surface roughness levels to be achieved that are less than 1 nm. Prior to conducting electroless nickel plating on the aluminum alloy mandrel of the X-ray focusing mirror, it is recommended to roughen the surface. Electroless nickel plating requires adherence to a number of strict specifications. First and foremost, the coating must have excellent adherence to the aluminum alloy matrix. Secondly, in order to provide an amorphous structure and homogeneous composition, the coating needs to have a phosphorus (P) percentage higher than 10%. Furthermore, there should be no flaws in the coating, and 150  $\mu\text{m}$  should be the ideal thickness. The physical drawing of chemical plating with Nickel–Phosphorus Alloy is shown in Figure 2.

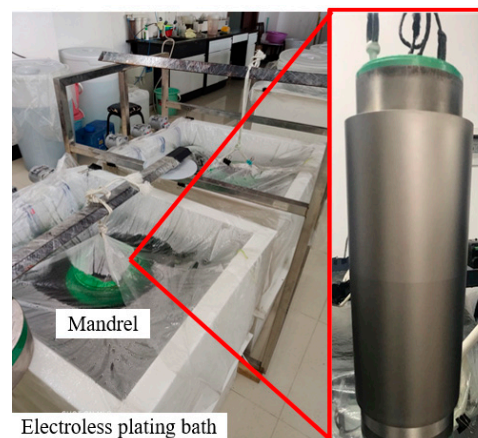


**Figure 2.** The electroless nickel plating bath and mandrel #24.

### 2.3. Ultra-Precision Turning Equipment and Process

The ultra-precision processing of the focusing mirror mandrel mold is the most critical step in the fabrication of the focusing mirror, because the surface topography of the focusing mirror mandrel mold will be directly mapped to the internal reflection surface. The working surface of the mandrel currently has the lengths of 300 mm with diameters ranging from 100 to 400 mm. The general ultra-precision turning machine tools are a single spindle and clamping with difficulty installing the workpiece, adjusting the coaxiality and controlling the turning taper. For the above reasons, the group has specially built an ultra-precision drum roll lathe to produce the mandrel mold. As shown in Figure 3, the ultra-precision turning machine DRL2000 (Harbin, China) could lathe shaft workpieces with a length of less than 2000 mm and a diameter of less than 500 mm. The X and Z axes are linear motion axes with a cross slider configuration. A liquid hydrostatic guide rail is adopted to ensure motion stiffness and smoothness. The characteristics of the C-axis include a precise angular displacement positioning and a high-speed spindle. A gas hydrostatic spindle is adopted to ensure high rotational accuracy and friction-free characteristics, and the bearing clearance is designed to meet the load and stiffness requirements. The machine tool's linear axis exhibits a static tracking error of  $PV < 10$  nm and a dynamic tracking error of  $PV < 20$  nm during machining operations. The chuck has a self-centering feature that allows each jaw to be adjusted individually to precisely position the roll shape. Ultra-precision turning uses natural single-crystal diamond tools and utilizes the inherent accuracy of ultra-precision machine tools to efficiently process shapes with a nanometer-level surface roughness and a sub-micron-level surface shape accuracy. Mold ultra-precision turning is responsible for quickly converging low-frequency errors. The turning process is divided into two steps. The first step is to roughly cut the mold blank to have a parabolic and hyperbolic profile. The cutting depth needs to consider the thermal expansion during electroforming and the residual thickness of the NiP layer. After the rough cut, the NiP layer is chemically plated on the mold surface. The second step is ultra-precision turning to ensure good contour accuracy and form a mirror surface, reducing the polishing time. Consequently, an experimental setup employed a circular diamond cutter, characterized by a 3 mm nose radius, a  $0^\circ$  rake angle, and a  $10^\circ$  clearance angle. The C-axis rotation velocity was set at 300 rpm. To produce the surface, a cutting depth of  $5\text{ }\mu\text{m}$  and a feed rate of  $5\text{ }\mu\text{m/rev}$  were implemented.

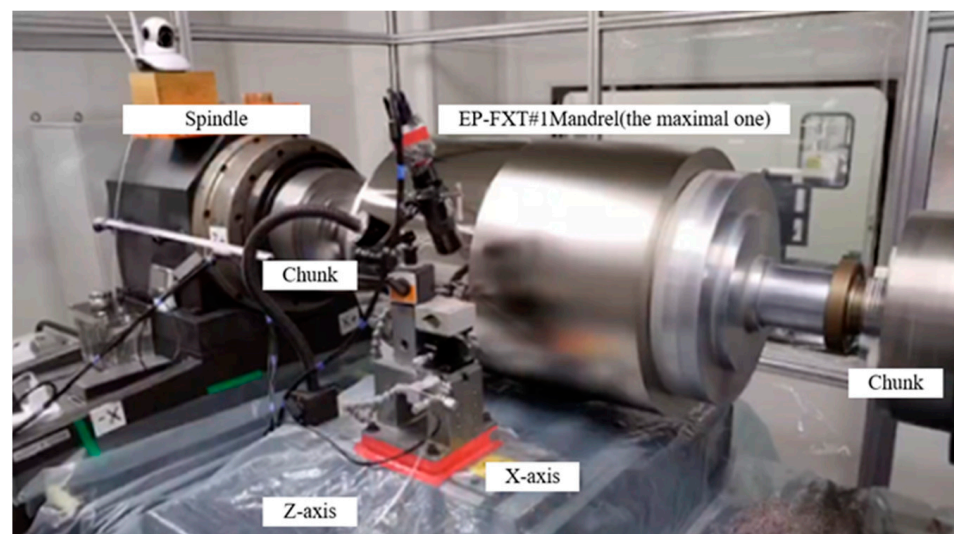


**Figure 3.** Schematic diagram of the DRL2000 with the EP-FXT #1 mandrel.



#### 2.4. Mandrels' Profile Accuracy Metrology

The mandrel of profile accuracy is an important indicator for evaluating the accuracy of focusing mirror molds and lenses. It reflects the deviation of the actual contour surface from the ideal contour surface, and the size of the error affects the focus angle resolution absolutely. In situ measurement technology is adopted to detect the surface shape accuracy of the mold. The advantage is that there is no need to install the focusing mirror mold twice, which greatly improves the detection efficiency and accuracy. The reverse measurement method is used to achieve a peak-to-valley (PV) turning generatrix accuracy  $< 0.2 \mu\text{m}$ . An in situ measurement device has been built based on the ultra-precision lathe. After adjustment, the system measurement error can be controlled within  $0.1 \mu\text{m}$  [16].

We use the inversion method to measure forward and backward twice to separate the mold busbar surface shape error from the machine tool motion error to improve measurement accuracy. The reversal method's measurement concept is depicted in Figure 4. Crucially, it is essential to highlight that the roller mold must undergo machining to remove the influence of its own shape error prior to executing the reversal method measurement. Typically, this method comprises two measurement stages. Initially, as illustrated in Figure 4a, the probe is positioned in front of the roller mold, where it scans the generatrix in a process referred to as the standard or normal scan. In the subsequent stage, the roller mold is rotated 180 degrees around the C-axis. Following this, the probe is installed behind the roller mold and re-scans the identical generatrix, as shown in Figure 4b. This scanning process is designated as the reversal scan. Throughout the measurement process, it is vital to maintain the probe at the same elevation as the roller mold's central line. The probe's output readings from these dual measurements can be denoted as

$$N(z) = S(z) + G(z) \quad (1)$$

$$R(z) = -S(z) + G(z) \quad (2)$$

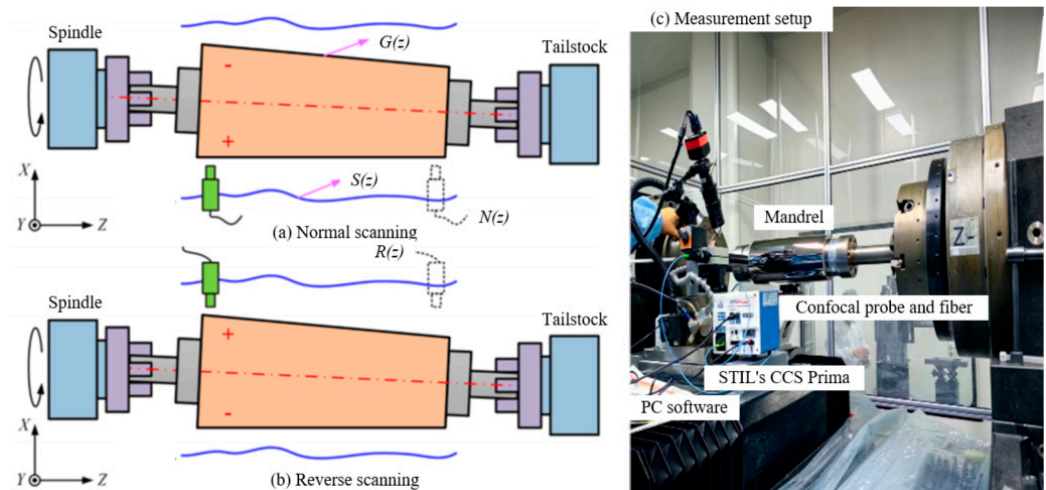


**Figure 4.** The inversion method for the mandrel.

In this context,  $N(z)$  denotes the outcome of the standard scanning process, whereas  $R(z)$  refers to the outcome of the inverse scanning operation.  $S(z)$  signifies the straightness along the Z-axis, and  $G(z)$  represents the taper present in the fabricated roller mold. In this scenario,  $z$  signifies the probe's position along the Z-axis during the measurement phase. Consequently, the taper of the manufactured roller mold can be expressed as

$$G(z) = \frac{N(z) + R(z)}{2} \quad (3)$$

Consequently, the measured outcomes via the inversion technique distinguishably isolate the machined roller mold's  $G(z)$  taper and the  $Z$ -axis'  $S(z)$  straightness. This derived taper, functioning as a correction factor, is incorporated into the subsequent NC turning program to rectify concentricity errors and enhance the roller mold's geometric precision.

In addition, a nanoscale white light confocal displacement sensor from the French STIL company is selected and the movement of an ultra-precision lathe is used to perform the contour scanning of the focusing mirror mold, as shown in Figure 4c. The probe is CL0-MG140 (Vaux-le-Pénil, France) with a maximum linear error of 16 nm and a background noise of 6 nm. In situ measurement can be directly inspected after mandrel turning, thereby avoiding secondary clamping errors. It is still crucial to compensate for the scanning motion errors of the machine tools. By employing the reversal method, the most influential guideway straightness error can be isolated. Furthermore, the in-situ reversal method is user-friendly, requires no additional testing environment and incurs low costs.

The typical results of mold cutting are illustrated in Figure 5, with the three measured generatrices evenly distributed along the circumference. Under stable environmental temperature conditions, the separated profile accuracy of the slide error is found to be  $PV < 0.2 \mu\text{m}$  along the entire length. Observing the guideway error separated from the EP mold measurements, the guideway error appears to be relatively flat, indicating that even without compensation, excellent cutting results can be achieved.

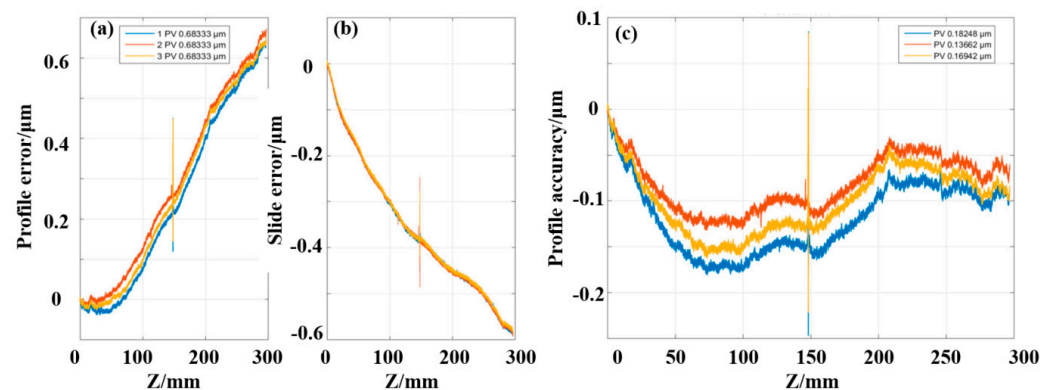


**Figure 5.** Typical turning generatrix profile. (a) Profile error. (b) Slide error. (c) Separated profile accuracy of slide error of EP#18.

### 2.5. The Bonnet Polishing and Full Aperture Pitch Polishing

Although single-point diamond turning (SPDT) can achieve a nano-scale surface roughness, it still cannot meet the total reflection requirements of X-ray wavelengths, especially for a hard X-ray. In addition, the surface after SPDT will leave uniform thread-like tool marks [15], which will cause a strong scattering of the incident light. Therefore, the ultra-smooth polishing process must be conducted to remove the tool marks on the turning surface and further improve the surface profile accuracy. Specifically, the discontinuity of the shape profile with a parabolic and hyperbolic shape at the mandrel mold edges and junctions leads to an increase in the polishing pressure and removal which cause slumping, and the form error, which depends on the polishing process, is generally around  $1 \mu\text{m}$  or higher. Ultra-smooth polishing of the mandrel mold can lead to collapses at the double edges of the mandrel mold and the middle of the interface, which can be replicated by the mirror. The edge effect error on the imaging system is disastrous for the degradation of W90. Hence, a combined polishing chain consisting of bonnet polishing and full aperture pitch polishing has been proposed, in which bonnet polishing is used to form generation, and full aperture pitch polishing plays a role in rapid surface smoothing, as shown in Figure 6.

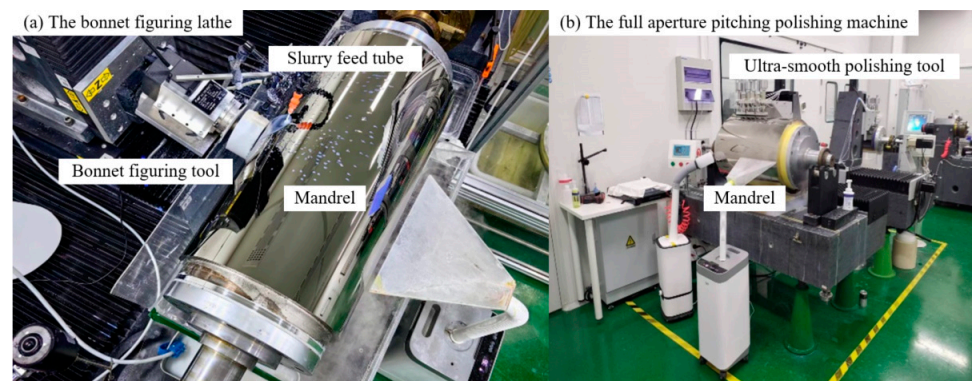


**Figure 6.** A combined polishing chain process.

## 2.6. Mandrels' Surface Microroughness Metrology

Currently, the focusing mirror molds are subjected to in situ and offline measurements to detect low-frequency errors. The mid-to-high-frequency errors of mirrors are measured using a white-light interferometer (Chotest SuperView WX 100, Shenzheng, China), and the roughness is measured using an atomic force microscope. Surface roughness is a key indicator of focusing mirror molds and mirrors, and it has an important impact on the final optical quality W90 of the focusing mirror. The CHOTEST (Shenzheng, China) white light interferometer, as shown as Figure 7a, is used to detect the roughness of the mold surface, and  $0.5\text{ mm} \times 0.5\text{ mm}$  is selected as the roughness evaluation area. The surface of the mandrel #24 detection result after polishing is shown in Figure 7b. It can be seen that the turning marks have been completely removed, and the surface has been super-polished to the roughness level of  $0.2\sim 0.3\text{ nm RMS}$  ( $500\text{ }\mu\text{m} \times 500\text{ }\mu\text{m}$ ) as shown in Figure 7c, which meets the ultra-smooth surface requirements. Atomic force microscopes (AFMs) are very sophisticated tools that enable the characterization of optical surfaces on very high spatial frequencies. An atomic force microscope consists of a probe with a metal tip a few micrometers thick, monitored by a laser beam. In order to obtain the final AFM results of the mirror, some test samples were cut from a #24-2 mirror and tested offline with a Bruker AFM as shown in Figure 7d; the microroughness rms value, which is the Sq value obtained directly, is  $0.41\text{ nm}$  ( $70\text{ }\mu\text{m} \times 70\text{ }\mu\text{m}$ ) measured with the AFM. Moreover, the lateral resolution of the measurement should be specified and calculated by the PSD. The high-spatial frequency, characterized by its random scattering effect on the spatial plane, is quantified by the power spectral density (PSD).

By employing the PSD functional method, HSF can be notably mitigated as shown in Figure 7e. PSDs were calculated from WX 100 ( $2.5\times$  and  $20\times$ ) measurements on mandrel #24 and the AFM ( $70\text{ }\mu\text{m} \times 70\text{ }\mu\text{m}$ ) measurements on the sample piece from cutting mirror #24. The target mandrel PSD of eROSITA is plotted for reference in the same range.

## 2.7. Mandrel Gold Deposition and Ni or NiCo Electroforming

Upon attaining the necessary polish and undergoing comprehensive cleansing, the mandrel is subjected to electroless nickel passivation. This involves stimulating the formation of a thin nickel oxide layer on its surface, an electrolytic procedure meticulously managed to achieve the optimal chemical composition. Thereafter, a  $100\text{ nm}$ -thick gold coating is applied through vapor or electrochemical deposition techniques [18]. After a thorough cleaning, the mandrel proceeds to undergo the vacuum deposition of a Au film. The precision in depositing this reflective surface is pivotal for the fabrication of grazing incidence optics in hard X-ray astronomy. Conventional X-ray telescopes for astronomy have employed relatively thicker coating layers ( $\sim 100\text{ nm}$ ) as they are devised for total reflection operation alone. The replication of the optical contour and the formation of the reflective surface are accomplished through the use of an RF magnetron sputtering apparatus as depicted in Figure 8. This gold layer serves as the definitive mirror image. Unlike Media Lario, which performed coating with a thin (approx.  $150\text{ nm}$ ) layer of Gold



by means of e-beam evaporation technology [4], we use magnetron sputtering technology to ensure the denseness and integrity of the gold film structure.

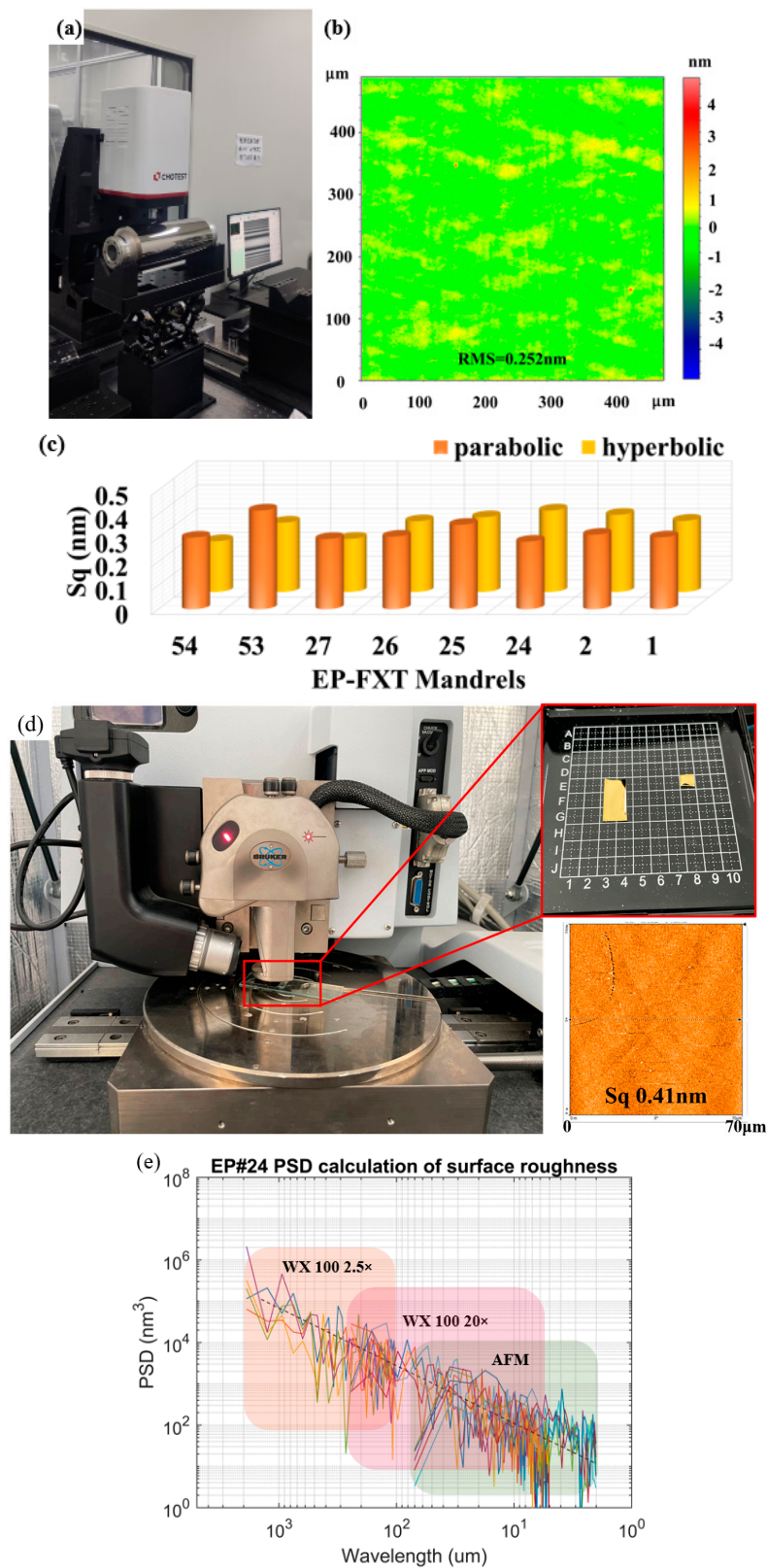


**Figure 7.** The metrology of the mandrel and mirror (cutting samples) of surface roughness. (a) the metrology equipment of the mandrel, (b) The surface roughness of the mandrel #24, (c) the roughness level, (d) AFM test and results, (e) PSD calculation.

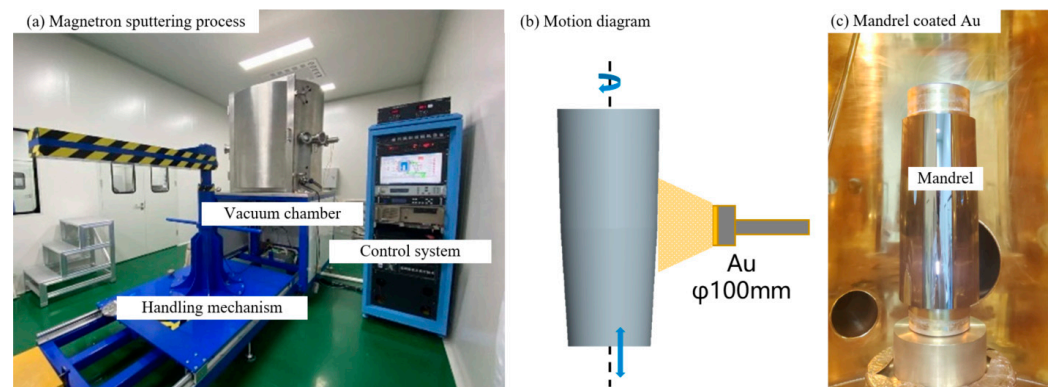


**Figure 8.** Mandrel gold deposition.

The progression and enhancement of the nickel–cobalt (NiCo) alloy in substitution for pure nickel in electroforming mirror substrates aim to enhance the alloy's mechanical strength and the optical efficiency of the mirror. The NiCo method was deeply investigated before by the NASA/Marshall group [19]. Internal stress, surface roughness and cobalt percentage have been the main characteristics observed. The most important requirements cover the yield strength, the microyield and Young's module of the axial to radial direction of the shell. The advantages in using the NiCo alloy instead of pure nickel are that (1) the NiCo alloy has a microyield point about three times higher than that of pure nickel; (2) the NiCo alloy has a higher hardness than pure nickel; (3) the NiCo alloy has a higher Ultimate Tensile Stress (UTS) compared to pure nickel; and (4) the NiCo alloy has a higher yield strength than pure nickel. A tailored stress-monitoring system, utilizing a diaphragm and a piezoelectric sensor, is employed to assess the stress during the electroforming of Ni or NiCo. As nickel deposits onto both the mandrel and the diaphragm, the minute distortion of the diaphragm, induced by stress, is amplified within a fluid chamber and detected by the transducer. The piezoelectric output is transformed into a voltage through a bridge circuit and subsequently fed into a computer for real-time process supervision. An algorithm governs the plating current, maintaining a zero-stress condition to guarantee that the fabricated mirror shell remains intact upon removal from mandrel. The procedure involves utilizing the mandrel as the cathode and the electroforming material as the anode; the electroforming solution comprises the metal salt solution containing the electroforming material. Under the influence of direct current (DC) voltage or a pulse current, the metallic ions present in the electroforming bath experience cathodic reduction, leading to the deposition of metal atoms, as shown in Figure 9. The thickness of the electroformed Ni or NiCo shell is controlled according to the power on the DC power supply, and the electroforming is stopped when the specified power is reached. After the electroformed part is out of the tank, it is slowly and evenly rinsed with pure water.

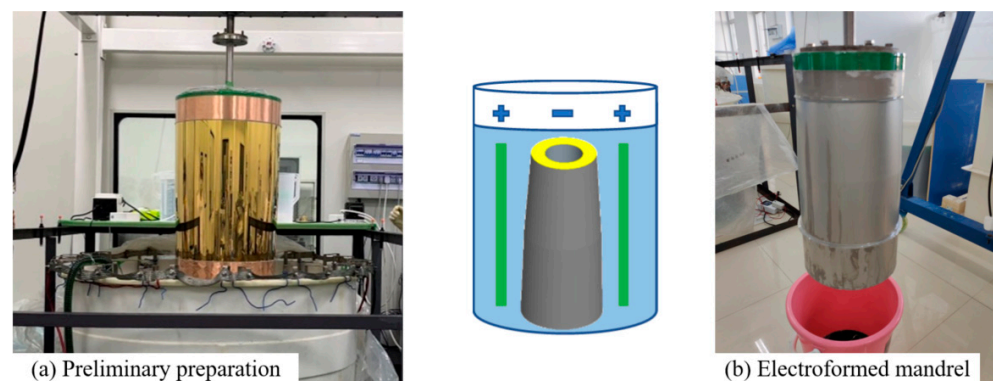


**Figure 9.** The electroformed nickel or NiCo process.

### 2.8. Demolding to Separate Mirror from Mandrel

The X-ray manufacturing process culminates in the critical demolding phase, which is pivotal for guaranteeing impeccable quality control. After the nickel substrate is electroformed, the electroformed nickel lens shell is separated from the mold by demolding, and the inner surface of the gold film is the reflection surface of the X-ray focusing mirror, thereby realizing replication manufacturing. A cryogenic method [20] is utilized to detach the shell from the mandrel. The disparity in expansion between the shell and the mandrel results in the creation of a minute gap, which occurs when liquid nitrogen fills the interior of the mandrel. The demolding device is shown in Figure 10. At the core of the mandrel release technique lies the application of liquid nitrogen into the interior of the mandrel. This action leads to an intense cooling of both the mandrel and the nickel coating, prompting them to experience elastic shrinkage as a response to the frigid temperatures. The contrasting thermal expansion coefficients between the nickel layer and the aluminum mandrel ensure that the mandrel's matrix contracts more significantly than the external nickel shell. The entire demolding process ensures a low humidity environment and monitors the mold temperature changes in real time. The gold-film nickel-matrix mirrors are separated from the mandrel, with the interior surface of the gold film serves as the X-ray reflector. Upon removal, the high-precision focusing mirror mandrel can be reused, enhancing fabrication efficiency and decreasing production expenses.

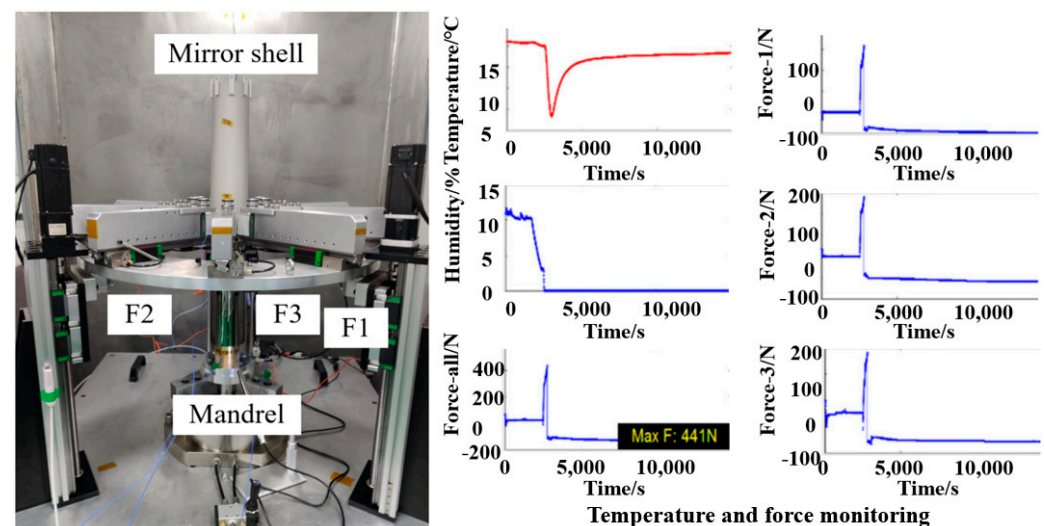


Figure 10. Demolding device.

### 2.9. Offline Generatrix Measurement of Mirror

To establish mutual verification with the in situ measurement method, we conducted a preliminary exploration of an offline measurement device for mirrors [21], as shown in Figure 11a. The measurement accuracy of this offline setup relies on the straightness, the installation precision of the vertical axis and the rotation and positioning accuracy of the turntable. The X-axis carriage is mounted on the Z-axis carriage, driven by a voice coil motor and guided by mechanical rails. The C-axis turntable utilizes a gas-static bearing, providing a radial runout of <50 nm and meeting the usage requirements. Owing to the constraints of the offline setup, we devised an innovative solution by encapsulating the laser source and optical elements within a unified enclosure to facilitate measurements on the mirror's interior surface. A cylindrical lens was employed to compensate for the optical spot deformation caused by the curvature of the mirror, thereby enhancing the measurement accuracy of the Position-Sensitive Detector (PSD) sensor. A combination of a semi-transparent mirror and a pentaprism was used to alter the reflection light path, minimizing the volume of the probe. With the optical lever measurement method, the designed measurement device is shown in Figure 11c and its principles are shown in



Figure 11b. This compact and ingeniously designed unit effortlessly accesses the innermost regions of the mirror shell housing for precise measurements.

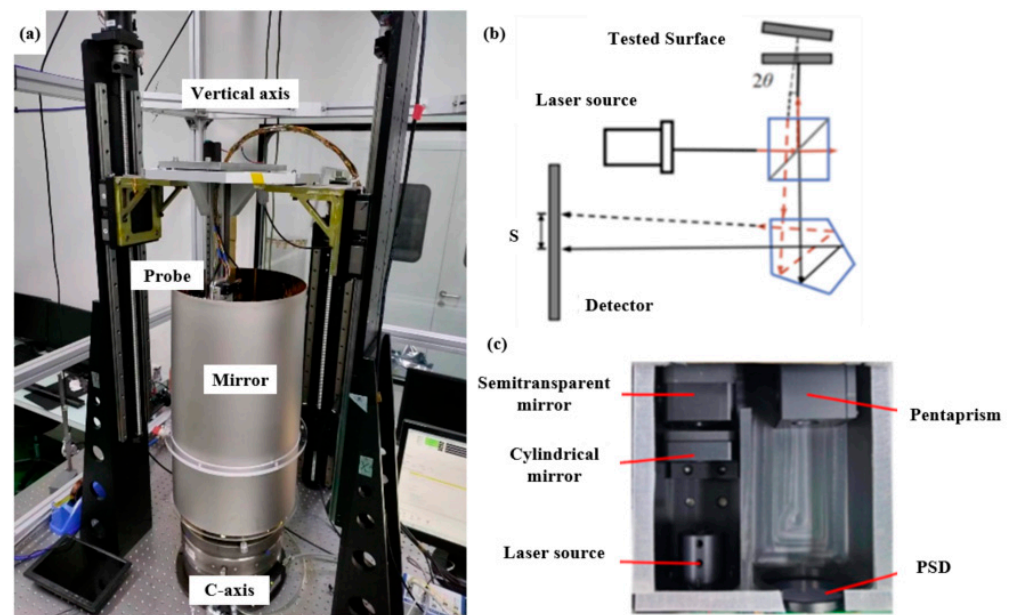


Figure 11. Offline measurement device.

The measurement repeatability and the generatrix measurement experiment were conducted as shown in Figure 12. The repeatability test involved measuring the same generatrix three times, revealing a repeatability error of less than 15 arcseconds. The measurement of both parabolic and hyperbolic surfaces was performed using a roundness measurement method, with adjacent cross-sections spaced 5 mm along the axial direction. The results of the experiments demonstrate that the constructed optical lever measurement device is capable of measuring the slope error of the mirrors and effectively capturing significant deformations and edge errors, as shown in Figure 12c.

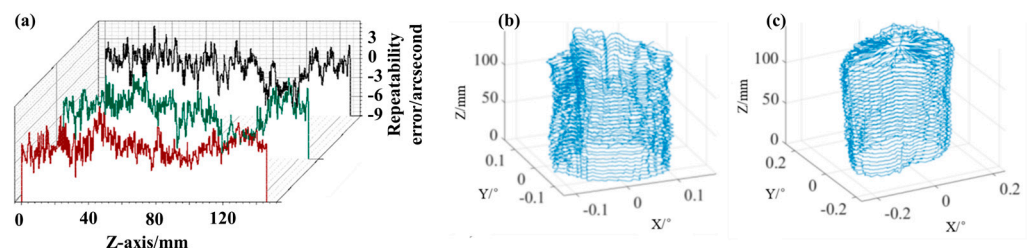


Figure 12. Optical lever measurement result of mirror. (a) Repeatability error. (b) Paraboloid test. (c) Hyperboloid test.

## 2.10. The Integration and Calibration of the Shells with Visible Light

As normally performed also by the other groups using electroforming technology, the integration in air of the confocal shells in the mirror module has been carried out using a UV light-testing optical bench. This allowed us to verify the reciprocal alignment of the mirror shells. It is mainly used just for performing the integration of the shells. Testing of the EP-FXT single-ply focusing mirrors is performed in a visible light test system with a parallel laser light source at 473 nm located on the bottom of the system, as shown in Figure 13. Suspended Optical Full Illumination Inspection, the method used for the testing and integration of the eROSITA telescope on board the SRG satellite [22], is also the method used for visible light testing in this paper, which allows for real-time, direct spot monitoring and sampling. The method can monitor and sample the spot in real time



and directly. The system is equipped with a parallel laser light source at 473 nm located at the bottom, as shown in Figure 13. During the test, the lens is lifted above the parallel light source by the device in the middle of the system, and the system uses a CMOS camera (Shenzhen, China) located on the top of the system for data acquisition, with a resolution of 4112 pixel  $\times$  2176 pixel, a pixel size of 3.45  $\mu\text{m}$ , a pixel size of 0.44", and a bit depth of 12 bit, which can satisfy the requirements for the acquisition of the spot data of the test lens.

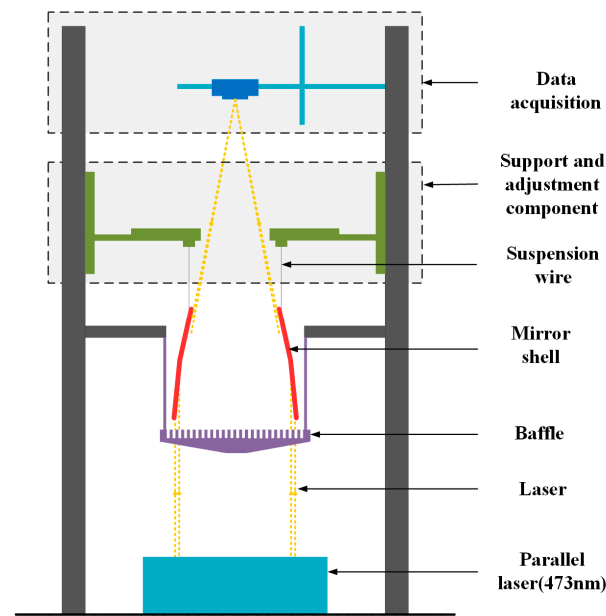


**Figure 13.** Diagram of the integration and calibration of the shells with visible light.

### 3. Results

#### 3.1. Mirrors and Engineering Model Integration

On the basis of the previous major background model tasks, the research team built a dedicated production base for X-ray focusing mirrors. Figure 14a,b shows the mandrel mold of the focusing mirror and the mirror after demolding. Upon the completion of the mirror shells' fabrication, the optical components must be integrated into a unique case. This instance guarantees adequate rigidity, enabling the optical module to be manipulated while minimizing the deformation of the enclosures. The integration of the mirror shells into the mechanical assembly is a critical task, given their extreme thinness and the high susceptibility to deformations [23]. Consequently, the implementation of specially designed front and rear support structures, featuring an extensive array of arms (not less than 20), as per prior research, becomes indispensable. To manage the fragility of the mirror shells and re-establish the optimal cylindrical shape, it is crucial to accurately fabricate two metal reinforcing rings for each shell, to be positioned at the upper and lower ends, as this was already performed for the telescope prototypes developed in Italy in the context of the SIMBOL-X/NHXM development program [24]. According to the optical design, the focusing mirrors of different sizes are assembled to form a nested focusing mirror group, as shown in Figure 14c.

As per plan C, which includes mainly demo parallel solutions, the team has also completed the development and a production of structural and thermal model (STM), a qualification model (QM) and a flight model (FM) of FXT mirrors for EP satellites, as shown in Figure 15.

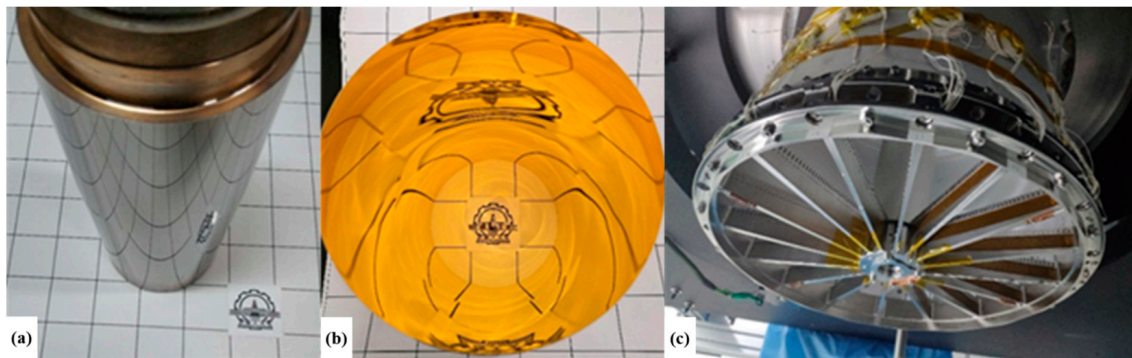


**Figure 14.** Productions. (a) Mandrel after demolding. (b) Mirror after demolding. (c) Mirror assembly.

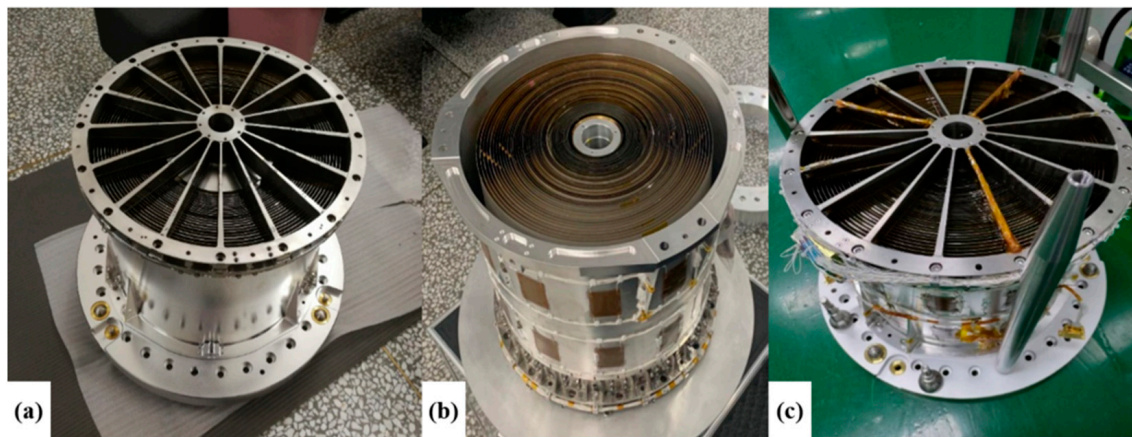


**Figure 15.** The models made in PRC for EP-FXT mirrors. (a) STM. (b) QM. (c) FM.

### 3.2. Visible Light Testing Results

X-ray focusing mirrors are made of 54 layers of nickel-plated gold that are precision-aligned by coaxial co-focusing with a visible-light mounting system. In the assembly integration process, the mirrors are tested to assess whether the quality of the mirrors meets the requirements of the assembly. The camera moves to the out-of-focus position to observe the spot, adjusts the spot to the center of the camera's field of view, adjusts the attitude of the lens by adjusting the lifting device so that its optical axis is coaxial with the parallel light source, moves the camera along the axis to collect the spot for out-of-focus testing to look for the smallest spot, and then calculates the angular resolution of the collected spot to match with the distance of the test camera and obtains the focal length and the angular resolution, as shown in Figure 16. The mirror angular resolution measured in UV light for the entire mirror module with the 54 integrated mirror shells, performed with the setup described above after the correction for diffraction, allowed us to perform some preliminary tests of the imaging quality of the optics. The inferred angular resolutions in terms of HPD and W90 are 48 and 134 arcsec, respectively. We are conscious that this is just a rough indication of the optics' quality in X-rays, as this method may be affected by important errors and does not account for the X-ray scattering. Additionally, these results illustrate that our technological effort is positively progressing.

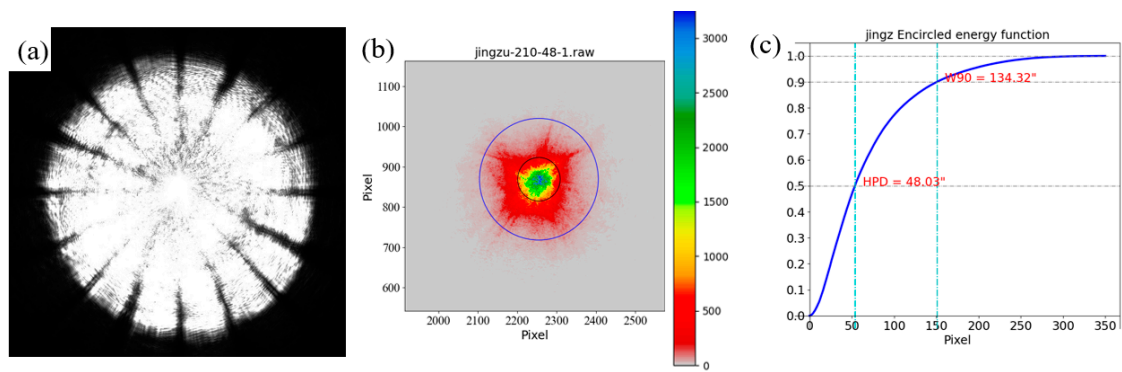


**Figure 16.** Results in a visible light test system with a parallel laser light source at 473 nm. (a) The intra-focal on-axis focal spot of 25 cm, (b) the focal plane, and the (c) encircled energy of the angular resolution for all the mirror shells of the FM.

### 3.3. X-ray Optical Testing Results

In order to further verify the manufacturing accuracy of the focusing lens, we directly perform X-ray optical tests on the lens to evaluate the manufacturing accuracy and performance of the focusing lens. The X-ray test of the focusing lens is carried out in the 100 m vacuum X-ray calibration device of the Institute of High Energy Physics of the Chinese Academy of Sciences. Its vacuum cavity is mainly composed of a large vacuum tank and a vacuum pipe. The large vacuum tank can be used for the overall test of the X-ray satellite payload to provide a quasi-parallel X-ray beam. The model is installed horizontally in the vacuum tank, as shown in Figure 17a. The X-ray light source is located at the far end of the vacuum pipe, enters the large vacuum tank through the vacuum pipe, and is focused on the camera after secondary reflection from the focusing mirror.

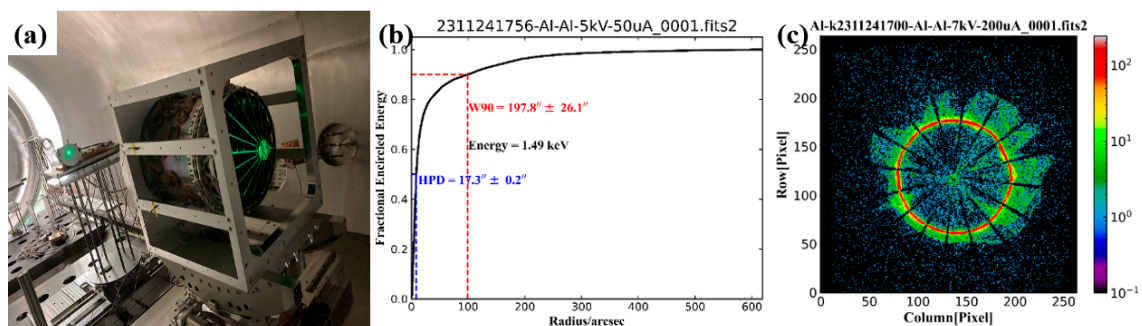


**Figure 17.** A test of the single shell #24 device and the results. (a) The model tested at IHEP/CAS. (b) The angular resolution of one mirror. (c) The defocus spot image.

The focusing mirror's efficacy is significantly determined by its angular resolution, which escalates with diminishing resolution measurements [25]. Specifically, the standard metric for angular resolution for X-ray focusing mirrors is the half-power diameter (HPD). Figure 17b shows that the angular resolution of single shell #24 is  $17.3^{\circ} \pm 0.2^{\circ}$  HPD,  $197.8^{\circ} \pm 26.1^{\circ}$  W90 @1.49 keV (Al-K line), which demonstrates the reliability and advancement of the process. Furthermore, the out-of-focus image of the mirrors and the visual characteristics of the spot shed light on the mirror's surface precision and circularity, as shown in Figure 17c. With reference to the X-rays properties in grazing incidence, a large effective area cannot be achieved through a single mirror, so it is necessary to use multiple confocal nested mirrors and possibly more replication of the same mirror module.

## 4. Conclusions

The X-ray focusing mirror is the core component of the X-ray astronomy satellite observation payload. Ultra-precision manufacturing technology of X-ray focusing mirrors

has always been a bottleneck factor restricting the improvement of China's astronomical observation and scientific research capabilities in the field of high-energy celestial objects. This article develops an independent and controllable X-ray focusing mirror electroforming replication method, and conducts a large number of explorations of the process and the equipment in the entire process chain. A comprehensive assessment has been conducted on the viability of the EP-FXT mirror module, confirming its capacity to fulfill scientific necessities. Nonetheless, additional technological advancements are required, which are currently being pursued:

- (1) Optimizations in the design and unique fabrication method for mandrels have been achieved, demonstrating the potential to attain form accuracy with a PV < 0.2  $\mu\text{m}$  and surface roughness at a sub-nanometer scale.
- (2) A dedicated production base for X-ray focusing mirrors had been implemented in China, and the first focusing mirror prototype had been successfully developed. The preliminary results are promising for achieving the basic performance requirements as a demo-parallel solution.
- (3) X-ray focusing mirrors are made of 54 layers of nickel-plated gold that are precision-aligned by coaxial co-focusing with a visible-light mounting system. The mirror angular resolution for entire mirror shells may be as good as 48 arcsec HPD, 134 arcsec W90 in a visible-light test system with a parallel laser light source at 473 nm.
- (4) The angular resolution of single shell #24 is 17.3 " $\pm 0.2$ " HPD, 197.8 " $\pm 26.1$ " W90 @1.49 keV (Al-K line), which illustrates that the domestically produced focusing mirrors have met the basic requirements of the project. Further hardware platforms are necessary to advance the technology, ensuring enhanced stability, processing capacity, and substrate dimensions in the subsequent stages.

**Author Contributions:** Conceptualization, B.W., D.W. and L.W.; methodology, F.D. and G.L.; software, F.D. and Y.W.; validation, J.X., Q.L. and K.W.; formal analysis, F.D. and Y.L.; investigation, J.X. and K.W.; resources, Y.Y. and Y.C.; data curation, J.X. and Q.L.; writing—original draft preparation, J.X.; writing—review and editing, W.C., Z.Q. and Y.J.; visualization, J.X.; supervision, B.W.; project administration, B.W.; funding acquisition, B.W. All authors have read and agreed to the published version of the manuscript.

**Funding:** This research was funded by the National Natural Science Foundation of China, grant number 42327802, the National Key R&D Program of China, grant number 2022YFB3403300, the State Key Laboratory of Mechanical System and Vibration, grant number MSV202313.

**Data Availability Statement:** Data is included within the article.

**Acknowledgments:** The authors thank Min Cong, Ke Yu, Jiawei Zhang and Yusa Wang for blue ray testing and thank Duo Li, Yuhao Li, Chunsheng Wu and Xudong Liu for WLI testing.

**Conflicts of Interest:** The authors declare no conflicts of interest.

## References

1. Yuan, W.M.; Zhang, C.; Ling, Z.X.; Zhao, D.; Wang, W.; Chen, Y.; Lu, F.; Zhang, S.-N.; Cui, W. Einstein Probe: A lobster-eye telescope for monitoring the X-ray sky. In Proceedings of the Space Telescopes and Instrumentation 2018: Ultraviolet to Gamma Ray, Austin, TX, USA, 10–15 June 2018; p. 10699.
2. Yuan, W.M.; Zhang, C.; Chen, Y.; Sun, S.; Zhang, Y.; Cui, W.; Ling, Z.; Huang, M.; Zhao, D.; Wang, W.; et al. Einstein Probe: Exploring the ever-changing X-ray Universe. *Sci. Sin. Phys. Mech. Astron.* **2018**, *48*, 039502. (In Chinese) [[CrossRef](#)]
3. Chen, Y.; Cui, W.; Han, D.; Wang, J.; Yang, Y.; Wang, Y.; Li, W.; Ma, J.; Xu, Y.; Lu, F.; et al. Status of the follow-up x-ray telescope onboard the Einstein Probe satellite. In Proceedings of the Space Telescopes and Instrumentation 2020: Ultraviolet to Gamma Ray, Online, 14–18 December 2020; p. 11444.
4. Friedrich, P.; Stieglitz, V.; Burwitz, V.; Eder, J.; Dennerl, K.; Hartner, G.; Langmeier, A.; Müller, T.; Rukdee, S.; Schmidt, T.; et al. X-ray optics test and calibration of the Einstein Probe Follow-up telescope. *Acta Astronaut.* **2024**, *221*, 255–265. [[CrossRef](#)]



5. Vernani, D.; Bianucci, G.; Grisoni, G.; Marioni, F.; Valsecchi, G.; Keereman, A.; Chen, Y.; Cong, M.; Yang, Y.; Wang, J.; et al. Follow-up x-ray telescope (FXT) mirror module for the Einstein probe mission. In Proceedings of the Space Telescopes and Instrumentation 2022: Ultraviolet to Gamma ray, Montreal, QC, Canada, 17–22 July 2022. [\[CrossRef\]](#)
6. Peres, C.B.; Fabian, A.C.; Edge, A.C.; Allen, S.W.; Johnstone, R.M.; White, D.A. A ROSAT study of the cores of clusters of galaxies—I. Cooling flows in an X-ray flux-limited sample. *Mon. Not. R. Astron. Soc.* **1998**, *298*, 416–432. [\[CrossRef\]](#)
7. Weisskopf, M.C.; Ramsey, B.; O'Dell, S.L.; Tennant, A.; Elsner, R.; Soffita, P.; Bellazzini, R.; Costa, E.; Kolodziejczak, J.; Kaspi, V.; et al. The Imaging X-ray Polarimetry Explorer (IXPE). *Results Phys.* **2016**, *6*, 1179–1180. [\[CrossRef\]](#)
8. Serlemitsos, P.J.; Soong, Y.; Chan, K.W.; Okajima, T.; Lehan, J.P.; Maeda, Y.; Itoh, K.; Mori, H.; Iizuka, R.; Itoh, A.; et al. The X-ray Telescope onboard Suzaku. *Publ. Astron. Soc. Jpn.* **2007**, *59*, S9–S21. [\[CrossRef\]](#)
9. Attina, P.; Alippi, E.; Casoli, P.; Lenti, A.; Monzani, F.; Poulsen, J.M. Overview of the SAX x-ray instruments development. In Proceedings of the SPIE—The International Society for Optical Engineering, Orlando, FL, USA, 19–21 April 1995. [\[CrossRef\]](#)
10. de Chambure, D.; Laine, R.; van Katwijk, K.; Kletzkine, P.; Valenzuela, A.; Grisoni, G.; Canali, M.; Hofer, S.; Tock, J.P.; Domken, I.; et al. Lessons learnt from the development of the XMM optics. *Int. Soc. Opt. Eng.* **1999**, *3737*, 2–17.
11. Brinkman, A.C.; Behar, E.; Güdel, M.; Audard, M.; den Boggende, A.J.F.; Branduardi-Raymont, G.; Cottam, J.; Erd, C.; den Herder, J.W.; Jansen, F.; et al. First Light Measurements with the XMM-Newton Reflection Grating Spectrometers: Evidence for an Inverse First Ionisation Potential Effect and Anomalous Ne A bundance in the Coronae of HR 1099. *Astron. Astrophys.* **2001**, *365*, 75–76. [\[CrossRef\]](#)
12. Burrows, D.N.; Hill, J.E.; Nousek, J.A.; Kennea, J.A.; Wells, A.; Osborne, J.P.; Abbey, A.F.; Beardmore, A.; Mukerjee, K.; Short, A.D.T.; et al. The Swift X-ray telescope. *Space Sci. Rev.* **2005**, *120*, 165–195. [\[CrossRef\]](#)
13. Citterio, O.; Campana, S.; Conconi, P.; Ghigo, M.; Mazzoleni, F.; Poretti, E.; Conti, G.; Cusumano, G.; Sacco, B.; Braeuninger, H.W.; et al. Characteristics of the flight model optics for the JET-X telescope onboard the Spectrum-X-Gamma satellite. In Proceedings of the Multilayer and Grazing Incidence X-ray/EUV Optics III, Denver, CO, USA, 4–9 August 1996; SPIE: Bellingham, WA, USA, 1996; Volume 2805, pp. 56–66.
14. Predehl, P.; Andritschke, R.; Arefiev, V.; Babyshkin, V.; Batanov, O.; Becker, W.; Böhringer, H.; Bogomolov, A.; Boller, T.; Borm, K.; et al. The eROSITA X-ray telescope on SRG. *Astron. Astrophys.* **2020**, *647*, A1. [\[CrossRef\]](#)
15. Dennerl, K.; Burkert, W.; Burwitz, V.; Freyberg, M.; Friedrich, P.; Hartner, G. Determination of the eROSITA mirror half energy width (HEW) with subpixel resolution. In *Space Telescopes and Instrumentation 2012: Ultraviolet to Gamma Ray*; Society of Photo-Optical Instrumentation Engineers (SPIE) Conference Series; Takahashi, T., Murray, S.S., den Herder, J.-W.A., Eds.; SPIE: Bellingham, WA, USA, 2012; Volume 8443, p. 844350.
16. Wu, K.; Ding, F.; Yang, Y.; Li, D.; Qiao, Z.; Qiang, P.; Wang, B. Influence on imaging performance and evaluation of Wolter-I type mandrel fabrication errors. *Appl. Opt.* **2022**, *61*, 6617–6626. [\[CrossRef\]](#) [\[PubMed\]](#)
17. Gubarev, M.; Ramsey, B.; O'Dell, S.L.; Elsner, R.; Kilaru, K.; McCracken, J.; Pavlinsky, M.; Tkachenko, A.; Lapshov, I.; Atkins, C.; et al. Development of Mirror Modules for the ART-XC Instrument aboard the Spectrum-Roentgen-Gamma Mission. In Proceedings of the Optics for EUV, X-ray, and Gamma-Ray Astronomy, San Diego, CA, USA, 26–29 August 2013.
18. Xue, J.; Liao, Q.; Liu, Y.; Wu, Y.; Jin, Y.; Wu, K.; Li, D.; Qiao, Z.; Ding, F.; Yang, Y.; et al. Precision polishing of the mandrel for X-ray grazing incidence mirrors in the Einstein probe. In Proceedings of the Advanced Optical Manufacturing Technologies and Applications 2022; and 2nd International Forum of Young Scientists on Advanced Optical Manufacturing (AOMTA and YSAOM 2022), Changchun, China, 29–31 July 2022; Volume 12507.
19. Gubarev, M.; Ramsey, B.; O'Dell, S.L.; Elsner, R.; Kilaru, K.; McCracken, J.; Pavlinsky, M.; Tkachenko, A.; Lapshov, I. The Marshall Space Flight Center development of mirror modules for the ART-XC instrument aboard the Spectrum-Roentgen-Gamma mission. In Proceedings of the International Society for Optics and Photonics, San Francisco, CA, USA, 21–26 January 2012.
20. Liao, Q.; Ding, F.; Chen, Z.; Li, D.; Wang, B. Study on the Fabrication Process of X-ray Focusing Mirrors. *Micromachines* **2023**, *14*, 1666. [\[CrossRef\]](#) [\[PubMed\]](#)
21. Wu, K.; Bao, X.; Ding, F.; Qiao, Z.; Chen, Z.; Li, D.; Liu, Y.; Xue, J.; Wang, W.; Li, Y.; et al. Diamond turning and full-frequency band error measurement methods for x-ray focusing mirror molds. In Proceedings of the Eighth Asia Pacific Conference on Optics Manufacture and Third International Forum of Young Scientists on Advanced Optical Manufacturing (APCOM and YSAOM 2023), Shenzhen, China, 29 December 2023; p. 12976.
22. Arcangeli, L.; Borghi, G.; Bräuninger, H.; Citterio, O.; Ferrario, I.; Friedrich, P.; Grisoni, G.; Marioni, F.; Predehl, P.; Rossi, M.; et al. The eROSITA X-ray mirrors: Technology and qualification aspects of the production of mandrels, shells and mirror modules. In Proceedings of the Society of Photo-Optical Instrumentation Engineers (SPIE) Conference Series SPIE, Rhodes Island, Greece, 4–8 October 2010; Volume 10565.
23. Vernani, D.; Borghi, G.; Calegari, G.; Castelnovo, M.; Citterio, O.; Ferrario, I.; Grisoni, G.; Moretti, S.; Valsecchi, G.; Brauning, H. Performance of a mirror shell replicated from a new flight quality mandrel for eROSITA mission. In Proceedings of the Optics for EUV, X-ray, and Gamma-Ray Astronomy V, International Society for Optics and Photonics, San Diego, CA, USA, 21–25 August 2011; p. 814707.

24. Basso, S.; Citterio, O.; Mazzoleni, F.; Pareschi, G.; Tagliaferri, G.; Valtolina, R.; Conconi, P.; Parodi, G. The problems concerning the integration of very thin mirror shells. In Proceedings of the SPIE Optical Engineering + Applications, San Diego, CA, USA, 2–6 August 2009; Volume 7437.
25. Wang, J.; Eder, J.; Ma, J.; Yang, Y.; Cui, W.; Yang, X.; Duan, X.; Feng, J.; Zhang, X.; Lu, B.; et al. The structural design and thermo-mechanical performance of the FXT for the EP mission. *Exp. Astron.* **2023**, *3*, 55. [[CrossRef](#)]

**Disclaimer/Publisher’s Note:** The statements, opinions and data contained in all publications are solely those of the individual author(s) and contributor(s) and not of MDPI and/or the editor(s). MDPI and/or the editor(s) disclaim responsibility for any injury to people or property resulting from any ideas, methods, instructions or products referred to in the content.